

This is a copy of the published version, or version of record, available on the publisher's website. This version does not track changes, errata, or withdrawals on the publisher's site.

Bragg edge tomography characterization of additively manufactured 316L steel

Matteo Busi, Efthymios Polatidis, Florencia Malamud, Winfried Kockelmann, Manuel Morgano, Anders Kaestner, Anton Tremsin, Nikola Kalentics, Roland Logé, Christian Leinenbach, Takenao Shinohara, and Markus Strobl

Published version information








Citation: M Busi et al. Bragg edge tomography characterization of additively manufactured 316L steel. *Phys Rev Materials* 6, no. 5 (2022): 053602.

DOI: [10.1103/PhysRevMaterials.6.053602](https://doi.org/10.1103/PhysRevMaterials.6.053602)

This version is made available in accordance with publisher policies. Please cite only the published version using the reference above. This is the citation assigned by the publisher at the time of issuing the APV. Please check the publisher's website for any updates.

This item was retrieved from **ePubs**, the Open Access archive of the Science and Technology Facilities Council, UK. Please contact epublications@stfc.ac.uk or go to <http://epubs.stfc.ac.uk/> for further information and policies.

Bragg edge tomography characterization of additively manufactured 316L steel

Matteo Busi ¹, Efthymios Polatidis ¹, Florencia Malamud,¹ Winfried Kockelmann ², Manuel Morgano,³ Anders Kaestner,¹ Anton Tremsin ⁴, Nikola Kalentics,⁵ Roland Logé ⁵, Christian Leinenbach ⁶, Takenao Shinohara,⁷ and Markus Strobl ^{1,*}

¹Paul Scherrer Institut, Laboratory for Neutron Scattering and Imaging, 5232 Villigen, Switzerland

²STFC, Rutherford Appleton Laboratory, ISIS Facility, OX11 0QX, Harwell, United Kingdom

³European Spallation Source, Partikelgatan 2, 224 84 Lund, Sweden

⁴University of California, Berkeley, California 94720, USA

⁵École Polytechnique Fédérale de Lausanne, 1015 Lausanne, Switzerland

⁶Swiss Federal Laboratories for Materials Science and Technology, 8600 Dübendorf, Switzerland

⁷J-PARC Center, Japan Atomic Energy Agency, 319-1195, Tokai, Japan



(Received 24 August 2021; accepted 13 April 2022; published 2 May 2022)

In this work we perform a neutron Bragg edge tomography of stainless steel 316L additive manufacturing samples, one as built via standard laser powder bed fusion, and one using the novel three-dimensional (3D) laser shock peening technique. First, we consider conventional attenuation tomography of the two samples by integrating the signal for neutron wavelengths beyond the last Bragg edge, to analyze the bulk density properties of the material. This is used to map defects, such as porosities or cracks, which yield a lower density. Second, we obtain strain maps for each of the tomography projections by tracking the wavelength of the strongest Bragg edge corresponding to the {111} lattice plane family. Algebraic reconstruction techniques are used to obtain volumetric 3D maps of the strain in the bulk of the samples. It is found that not only the volume of the sample where the shock peening treatment was carried out yields a higher bulk density, but also a deep and remarkable compressive strain region. Finally, the analysis of the Bragg edge heights as a function of the projection angle is used to describe qualitatively crystallographic texture properties of the samples.

DOI: [10.1103/PhysRevMaterials.6.053602](https://doi.org/10.1103/PhysRevMaterials.6.053602)

I. INTRODUCTION

Over the past two decades, neutron Bragg edge imaging has seen rapid development and numerous applications in many different fields [1]. This imaging mode uses pulsed beams with a suitable time-of-flight structure, which can be resolved, e.g., by novel time-of-flight imaging detectors. A recent widely used detector integrates a pixelated Medipix/Timepix readout chip into a microchannel plate electron multiplier [2]. The conversion from time-of-flight of the neutrons to wavelength enables additional imaging modalities compared to the conventional attenuation-based contrast mapping. Several multimodal studies included the imaging of lattice strains [1,3,4], crystalline phase composition [1,5], and texture variations [6,7]. The extension to volumetric 3D analyses through tomography scans was demonstrated for the reconstruction of 3D maps of crystalline phase transition from austenitic to martensitic stainless steel [8]. However, the 3D reconstruction of strain fields has proven to be a more complex task. The main challenge is that the tensorial nature of strain prohibits the application of standard tomographic reconstruction techniques. For example, for a sample with anisotropic strain, knowing that for a projection the strain tensor component is along the neutron beam direction, a rotation of the sample would change the tensor component that is probed by the neutron beam. However, under certain assumptions on

symmetrical properties of the lattice strains in the sample, the reconstruction of strain fields has been demonstrated and proven feasible [9,10]. More recently, Hendricks *et al.* have shown that using forward models a generalized approach for the reconstruction of the tensorial components of the strain field could be applied [11].

Many applications of neutron characterization with diffraction [12–18] as well as white beam attenuation contrast neutron imaging [19,20] and neutron grating interferometry [21–23] can be found in the field of additive manufacturing (AM). These different techniques cover different aspects and complement each other, and can be integrated simultaneously as shown in [24] where the setup allows for an *in situ* combination of multimodal neutron imaging with neutron diffraction. The main advantage of these techniques is that they are nondestructive and that in contrast to x rays, neutrons have high penetration depth in certain metallic compounds. One of the critical aspects of parts processed through AM is the build up of strains caused by the complex thermomechanical process [25]. A powerful post-processing treatment for the relief of such strains is laser shock peening (LSP), which is applied to the top surface of the built parts [26]. A novel AM material processing technique, namely 3D laser shock peening (3D-LSP), combines laser powder bed fusion (LPBF) with LSP treatments at intermediate layers [27]. The purpose of this combined technique is to introduce beneficial compressive strains (CS) that counteract the formation of the tensile strains (TS), which build up particularly in the

*markus.strobl@psi.ch

surface regions. Furthermore, this technique enables tailoring the strain field according to predefined models in an LPBF built component. The introduction of CS in a component is suited to enhance the material's lifetime, prevent cracking and distortions [28]. It has been shown that 3D-LSP has the ability to, e.g., introduce CS deeper into the sample, when compared to single surface layer LSP treatments [29]. Due to the layer-by-layer nature of the processing method and in particular also for alternate changes of the laser scanning direction, the strain tensor can be assumed isotropic in a plane orthogonal to the build direction. Based on this assumption, the strain profiles of as built and LSP-treated LPBF stainless steel 316L samples were characterized with Bragg edge radiography. The results and initial assumptions were validated by comparing the residual stress values measured with the conventional destructive hole-drilling method [30]. Subsequently, using Bragg edge radiography, parametric studies of LPBF processing parameters were carried out for a large series of samples [31]. However, by radiographic imaging, the strains are measured as averages along the sample thickness parallel to the neutron beam direction hence, strain variations along the sample thickness are obscured. Here we show how multiple radiographs collected from different angles can be used for tomographic reconstructions, and reveal elastic strain variations in a 3D volumetric map.

In this work we perform neutron Bragg edge tomography of a 3D-LSP processed sample, and one as built by LPBF with identical processing parameters. First, we consider conventional attenuation tomography of the two samples by integrating the signal for neutron wavelengths beyond the highest wavelength Bragg edge, where the linear trend of the attenuation coefficient enables us to probe the bulk density of the material. This is used to map defects and parts of the sample with lower density, caused, e.g., by porosity. Second, the wavelength of the strongest Bragg edge corresponding to the {111} lattice planes is used to obtain a strain map for each projection of the tomography scan. An iterative algebraic reconstruction is used to obtain volumetric 3D maps of the strain in the bulk of the samples, which is further converted into 3D strain maps. The approach for the reconstruction of volumetric strain can be applied to different families of lattice planes, however, in the present study we only report the results for {111} as it exhibits the best contrast and signal to noise ratio in the strain maps and also due to the fact that the AM-processed material is not texture free. It is known that for texture-free fcc metals, typically the {311} family of planes is used for residual stress characterization, as it is the least affected by intergranular stresses [32]. It is noted that the choice of the most appropriate lattice plane families for residual stress evaluation, due to intergranular stresses in textured AM materials, is not within the scope of the present work. Finally, the analysis of the Bragg edge heights as a function of the projection angle is used to evaluate qualitatively symmetric properties in the crystallographic texture of the samples.

II. METHODS AND EXPERIMENTS

A. Theoretical background

In neutron Bragg edge imaging, the wavelength (λ) dependent attenuation spectrum $\mu(\lambda)t = -\log[I(\lambda)/I_0(\lambda)]$ is

measured, where $I_0(\lambda)$ and $I(\lambda)$ are the incident and transmitted neutron beam spectra through the sample, μ is the linear attenuation coefficient, and t is the sample thickness. The attenuation contains contributions from cross sections of absorption and scattering. The absorption cross section, which becomes dominant for longer wavelengths (e.g., above 4.2 Å for the stainless steel 316L examined here, see Fig. 4), has a linear dependence on the wavelength. Therefore, it can be used to efficiently measure the bulk density, in particular in this wavelength regime where the scattering contributions can be neglected. The scattering cross section, and especially the elastic coherent component, dominates in the shorter wavelength thermal neutron regime for certain crystalline materials (e.g., Cu, Fe, Zr) and reflects crystallographic properties. Bragg edges, which are the characteristic features of the wavelength dependent scattering cross section of these polycrystalline materials, appear as sharp discontinuities in the attenuation spectrum and they can be considered as the corresponding Bragg peaks in diffraction. The wavelength of those discontinuities are related to the individual lattice plane families through Bragg's law. For a specific family of lattice planes with lattice spacing d_{hkl} , Bragg's law relates the neutron wavelength λ to the Bragg angle θ between the beam and the lattice planes as $\lambda = 2d_{hkl} \sin(\theta)$. The Bragg angle increases with the wavelength until it reaches $\theta = \pi/2$. Beyond the corresponding wavelength $\lambda = 2d_{hkl}$ the Bragg condition for the specific lattice plane family $\{hkl\}$ cannot be satisfied any longer and there is a corresponding sharp drop in the attenuation spectrum. The wavelength at which the Bragg edge occurs can be thus considered a measure of the lattice spacing $d_{hkl} = \lambda_{hkl}/2$. The full pattern of the Bragg edges for the different hkl lattice planes is unique to each crystal structure and can thus be used for their discrimination or for the characterization of material crystalline phase transformations. Finally, the shape of the spectra and height of Bragg edges carry microstructure information such as crystallite size and crystallographic texture. In particular for textured materials, the shape and height of the Bragg edges change drastically with the orientation of the sample in the beam and from the quantitative analysis of such changes, it is possible to extract texture information. In this work we utilize Bragg edge measurements for the characterization of elastic lattice strain ϵ_{hkl} in the direction parallel to the neutron beam. Elastic lattice strain can be expressed as the relative deviation of the lattice spacing d_{hkl} from a reference lattice spacing d_{hkl}^0 :

$$\epsilon_{hkl} = \frac{d_{hkl} - d_{hkl}^0}{d_{hkl}^0}. \quad (1)$$

Methods for obtaining reliable strain-free d_{hkl}^0 values are given in [33]. The magnitude of strain is referred as micro (1×10^{-6}) strain ($\mu\epsilon$). Crystallographic texture effects challenge the wavelength tracking of Bragg edge, in particular for effects that distort strongly the shape of an edge. For such cases, the common methods used for fitting such as peak profile or derivative peak fitting suffer significantly from pixel-to-pixel variations. However, for the neutron beam directions measured in this paper, the effect of the crystallographic texture of the samples yields exclusively Bragg edge height variations.

B. Materials and instrumentation

The two samples examined in this work are rectangular cuboid samples made of austenitic stainless steel 316L (i.e., Fe-17Cr-12Ni) processed with LPBF. The samples were produced using MetcoAdd spherical powder (Oerlikon Metco, Switzerland) with mean diameter $31.86 \mu\text{m}$ and a Concept M2 machine (Concept Laser GmbH, Germany). The machine is equipped with a fiber laser operating in continuous mode with a Gaussian intensity distribution and a wavelength of 1070 nm and a spot size ($1/e^2$) of $90 \mu\text{m}$. The laser power, hatch distance, and powder layer thickness were kept fixed to 125 W , $105 \mu\text{m}$, and $30 \mu\text{m}$, respectively. The laser speed of the LPBF processing was set to 300 m/s , and a 3 mm thick support structure was used and subsequently cut via electrodischarge machining. The samples were produced under N_2 atmosphere and the O_2 content was kept below 1% during the process. One of the two samples was produced by conventional LPBF and left in as a built condition (AB). The other sample was produced involving the novel 3D-LSP technique. Stopping the LPBF process 20 layers before the scheduled end, half of the intermediate sample surface was treated with LSP and then the LPBF process was continued. Additionally, on the final layer, the same half of the sample surface was treated with LSP. During LPBF, the strategy adopted for the laser scanning direction was alternating two orthogonal scanning orientations in a checkerboard pattern, which was repeated for each printed layer. With respect to the LSP treatment, the laser energy was set to 1.5 J corresponding to a laser areal power density of 30 GW/m^2 . Finally, the area overlap between two successive laser beam footprints in LSP applied to the surface was 80% . Additionally, another AB sample was annealed at a temperature of 1000°C for 10 min , serving as an unstrained reference sample. The annealing treatment is considered not to have influenced any chemical segregation that would affect the lattice parameter. For this sample, the reference lattice spacing d_{hkl}^0 was measured as 2.0725 \AA from a single Bragg edge radiography and compared with powder and an annealed sample value obtained with neutron diffraction. All measured d_{hkl}^0 values agree within an uncertainty range of $150 \mu\epsilon$.

The tomography scan of the two samples was performed at the RADEN beamline at J-PARC (Japan), which is well suited for neutron Bragg edge imaging [34]. The sample was rotated with the rotation axis parallel to the LPBF build direction, in 19 angular steps following the golden ratio rule [35,36]. This choice was made to optimize the angular coverage with a relatively low and in particular uncertain total exposure time available. Each projection was exposed for 1 h for recording transmission spectra in all pixels of the imaging detector. RADEN uses a spectrum that ranges up to 8.8 \AA with a wavelength resolution of $\Delta\lambda/\lambda < 0.2\%$ for wavelengths above 3 \AA [34]. For the tomography acquisition, the wavelength spectrum range selected was between 1.8 and 5.3 \AA . Table I highlights all relevant Bragg edges specific to 316L stainless steel that are accessible by the neutron source spectrum. The wavelength bin width was set to 4.3 m\AA , which is approximately half of the instrumental resolution at 4.1 \AA . For each of the projections scanned, we localized pixelwise the wavelength of the Bragg edge corresponding to the $\{111\}$ lattice planes, by calculating the centroid of the derivative of

TABLE I. List of theoretical Bragg edges within the neutron source spectrum utilized, considering a lattice parameter of 3.60 \AA , after [37].

Lattice planes:	(222)	(311)	(220)	(200)	(111)
Neutron wavelength (\AA)	2.07	2.16	2.54	3.59	4.15

the attenuation spectrum, in a 0.5 \AA wide wavelength band around the respective Bragg edge. In this way, images of both the attenuation and the $\{111\}$ Bragg edge wavelength were obtained for each projection. The Bragg edge wavelength maps were further converted into elastic lattice strain using Eq. (1) and a reference d_{hkl}^0 value measured from the annealed sample in the same manner.

Furthermore, the bulk textures of the samples were determined on the General Materials (GEM) neutron diffractometer [38] at the ISIS pulsed neutron source, UK. A polychromatic neutron beam of $20 \times 15 \text{ mm}^2$ (height \times width), so the whole sample was in the beam. The neutron wavelengths were between 0.2 and 3.5 \AA , with a collection time of 30 min . In order to reconstruct the orientation distribution function (ODF), time-of-flight diffraction data were collected for one sample orientation taking advantage of the large angular detector coverage. Post experiment, 6500 individual detector elements on GEM were grouped into 160 discrete segments, such that each segment covered angles of about $10 \times 10 \text{ deg}$ [38]. The diffraction patterns were normalized to the wavelength distribution of the GEM neutron beam and the MAUD analysis software [39] was employed for texture analysis by Rietveld fitting 20 Bragg peaks in each detector segment. The extended Williams-Imhof-Matthies-Vinel (E-WIMV) algorithm implemented in MAUD was used for extracting the ODF with a resolution of 10 deg , matching the angular detector resolution. Pole figures were recalculated from the ODF and plotted in MTEX [40], with pole densities expressed as multiples of a random distribution (m.r.d.).

C. Tomographic reconstruction

For the volumetric reconstruction of the 3D strain map, two individual sinograms are obtained by calculating: (i) The attenuation map of each projection, $-\log \frac{I(u,v,\omega)}{I_0(u,v,\omega)} = \mu(u,v,\omega)t(u,v,\omega)$, by integrating $I(\lambda)$ and $I_0(\lambda)$ for all wavelength bins above 4.2 \AA . u and v are the pixel coordinates and ω is the rotation angle of each projection. (ii) The lattice spacing map of each projection $d_{hkl}(u,v,\omega)$. This map is multiplied to the first one to obtain $\tilde{d}_{hkl}(u,v,\omega) = d_{hkl}(u,v,\omega)\mu(u,v,\omega)t(u,v,\omega)$, which is again the line integral of the attenuation, but now scaled by the average lattice spacing value. This step is necessary because standard tomographic reconstruction algorithms are based on line integrals, whereas the measured lattice spacing is a quantity averaged along the neutron beam path. At this point, the two sinograms are both processed using the same reconstruction algorithm to obtain volumetric 3D maps of the attenuation $\mu(x,y,z)$ and the lattice spacing multiplied by the attenuation $\tilde{d}_{hkl}(x,y,z)$, where x , y , and z are Cartesian coordinates respective to the

sample. Finally, the actual lattice spacing 3D map is retrieved by a voxel-by-voxel division of the two tomographic reconstructions $d_{hkl}(x, y, z) = \tilde{d}_{hkl}(x, y, z) / \mu(x, y, z)$. The result is then converted to elastic strain using Eq. (1). The following assumptions are considered, which makes it possible to reconstruct the lattice strain volume: (i) the strain is isotropic, i.e., with equal x and y components in planes perpendicular to the build direction; (ii) the sample has weak texture variations [see Fig. 4(a)]. The first assumption is required since the strain is measured in the direction of the beam, which changes according to the projection rotation angle. The second assumption ensures that texture effects do not interfere with the Bragg edge wavelength tracking, when the sample is rotated.

The reconstruction algorithm used is the simultaneous iterative reconstruction technique, available in the ASTRA toolbox [41]. This algorithm is well suited to suppress the reconstruction artifacts due to a limited number of projections, such as in this case. For the reconstructions, a spatial rebinning of two-by-two pixels was carried out to improve the fitting performance, leading to a voxel size of $110 \times 110 \times 110 \mu\text{m}$ in the reconstructions. Alternatively and similarly to the method presented here, one could perform the conventional volumetric reconstruction for each of the wavelength bins of the neutron Bragg edge tomography scan and then localize the Bragg edge wavelength for each voxel (x, y, z) as demonstrated by Carminati *et al.* [42]. In terms of performance, we found comparable results by using the two different approaches. The advantage of using one or another is purely due to computing time. When a high number of wavelength bins and voxels of the reconstructed volume are chosen, the spectral method [42] can become dramatically slow, due to the high amount of both reconstructions and wavelength tracking to be performed. On the other hand, since wavelength tracking is carried out on a pixel-by-pixel basis (or voxel-by-voxel, respectively), when the total amount of pixels in the projections is higher than the reconstructed sample voxels, the method presented here can become slower. However, so far in most of the cases of Bragg edge tomography a limited number of projections is usually chosen, with a high exposure time for each, due to the relatively low signal to noise ratio of the technique for which a high wavelength resolution is desired.

III. RESULTS AND DISCUSSION

Figure 1 shows the reconstructed 3D maps of the strains for the sample manufactured with conventional LPBF in as built (AB) condition, and the sample partially treated with the 3D-LSP technique. The volumes clearly display the typical strain behavior of LPBF samples along the build direction (z). The positive values in the proximity of the bottom and top edge surfaces, corresponding to TS (red color), rapidly turn into a plateau of negative values, corresponding to CS (blue color), at the bulk center of the sample. The portion of the sample surface that was treated with 3D-LSP shows a localized zone of CS at the top of the sample, with the corresponding TS being pushed deeper into the sample. This effect is stronger towards the center of the sample. The figure also shows in the bottom row a segmentation of TS regions, in order to better visualize the effect of the 3D-LSP treatment on the sample

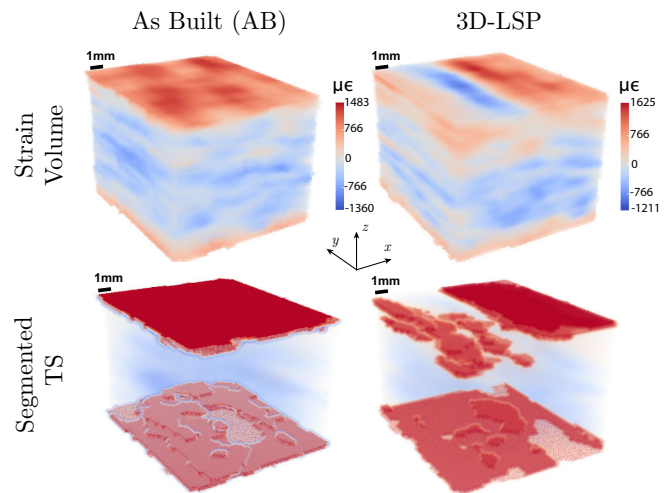


FIG. 1. Top row: Reconstructed strain volumes corresponding to the as built (AB) sample (left) and the one partially treated with 3D-LSP (right). The color map goes from blue (CS) to white (zero strain) to red (TS). The build direction is aligned to the z axis. Bottom row: The samples' respective segmented TS regions, achieved by a binary threshold between 500 and 1500 $\mu\epsilon$.

surface. This was achieved by a binary thresholding of values between 500 and 1500 $\mu\epsilon$, and displaying the resulting voxels with full opacity.

To evaluate the enhancement of the material's mechanical properties when using the 3D-LSP processing technique, it is important to quantify the magnitude of CS introduced in the treated partial volume of the sample, and the depth at which the strains convert to TS. Figure 2 shows plots of the strains for specific regions of the samples, which were calculated by taking the corresponding average strain value of each volume slice orthogonal to the build direction, as a function of the sample height. For the as built sample, the whole reconstructed volume was considered, whereas for the

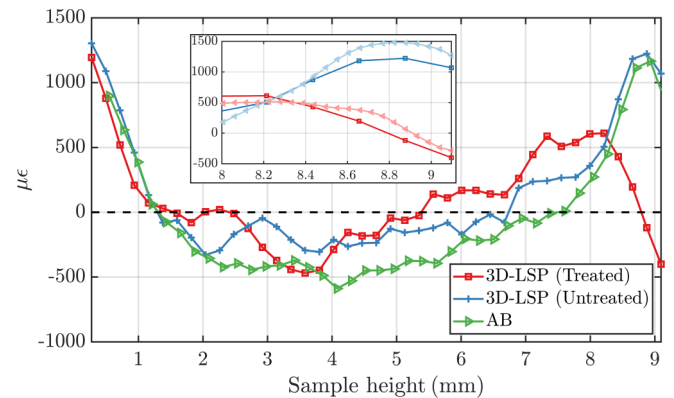


FIG. 2. Vertical profiles of the strain as a function of sample height for the as built (AB) sample and the 3D-LSP treated and left as built regions of the treated sample. In the inset graph, the same lines corresponding to the 3D-LSP samples (square marker), are compared to the results obtained with radiography, with same color code but lighter tone (triangle marker). Note that the LSP-treated region is at the higher sample height.

3D-LSP treated sample two regions were taken, respective to the untreated and treated halves. The vertical profiles towards the bottom of the samples are similar for each of the regions with a maximum TS of around $1300 \mu\epsilon$ and a conversion depth to CS at approximately 1.3 mm from the bottom. A comparable TS behavior is found for the top AB sample surfaces, with a conversion depth to CS of approximately 1.7 mm from the top. The discrepancy between the CS depths at the two sides is an expected result, which compares well with the extensive Bragg edge radiography studies and hole-drilling method [31]. The principal reason behind this is thought to be the electrodischarge machining cutting of the support structure, resulting in a release of the TS at the corresponding side of the sample. With respect to the 3D-LSP treated surface, the sample shows a surface CS of approximately $-480 \mu\epsilon$, which converts to TS at about 0.2 mm from the surface, then, it rises up to a 1.5 mm deep plateau of $518 \mu\epsilon$ and finally converts back to CS at approximately 4 mm from the top surface. Figure 2 also contains corresponding vertical profiles of the strains of the same samples measured with standard radiographic neutron Bragg edge imaging [43]. A comparison of the results obtained with tomography and radiography yields very similar results for the AB sample. Regarding the 3D-LSP treated surface, while the surface CS magnitude is nearly identical for the two measurements, the strain values below the depth at which they convert to TS appears higher for the tomography measurement. This may be caused by edge artifacts due to the severely limited number of projections, which introduces a positive bias in the retrieved elastic lattice strain calculated. However, all trends of the strain variations produced by the 3D-LSP treatment are well captured and comparable between radiography and tomography, demonstrating the feasibility of strain tomography for corresponding investigations.

As discussed in the previous section, not only the strain volumes are reconstructed from the tomography scan, but also the linear attenuation coefficient. Figure 3(a) depicts the attenuation reconstruction of the two samples, where no major differences between the two samples are observed as both yield overall similar density values. However, thresholding of sample voxels with lower attenuation reveals the spatial localization of sample zones with lower bulk density, due to porosity. It has to be noted that in literature, for materials with similar processing conditions, the pore sizes are reported to be varying, depending on the LPBF settings, from a few to a few hundred μm [44]. Hence, our detector's pixel pitch of $55 \mu\text{m}$ only allows for the detection of clusters of neighboring pores or relatively large pores. Figure 3(b) shows the vertical profiles of the average bulk density calculated from the linear attenuation coefficients, for the corresponding 3D-LSP and AB parts of the samples. It is observed that the 3D-LSP processing, in addition to introducing CS, serves the purpose of increasing the bulk density by closing of pores, an effect that has also been reported in literature [27,45]. It is found that up to 2 mm deep into the sample from the top surface, the bulk density is increased by approximately 2%.

Finally, we have examined the Bragg edge spectra of the bulk AB sample for each of the tomography projections. We have observed that by rotating the sample around the build

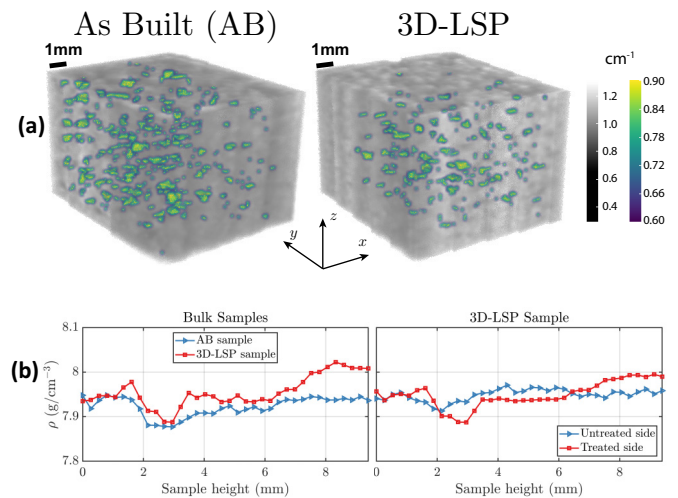


FIG. 3. (a) Volumetric 3D reconstruction of the linear attenuation coefficient (cm^{-1}) of the AB and 3D-LSP samples. Overlapped are regions of the samples with lower attenuation, by thresholding between 0.6 and 0.9 cm^{-1} . (b) Vertical profiles of the average bulk density (g/cm^3) along the build direction (z) for the bulk AB and 3D-LSP samples, and the treated and untreated parts of the latter.

direction, the relative Bragg edge heights vary symmetrically with a 90° period. This type of symmetry is typically found for chessboard (or island) LPBF scanning strategy [46,47], as the one used for the samples examined in this work. Figure 4(c) shows the Bragg spectra for a selection of seven projection angles: -85.0° , -42.5° , -22.4° , 0° , 52.5° , 72.6° , and 82.6° . The spectra have been normalized to have equal values between 4.2 and 5 \AA , to take into account the different neutron path lengths for different projections, assuming no contributions from the texture are to be found in this wavelength regime. While the angles are not equidistant due to the choice of golden ratio tomography for the projection angles, it can be observed easily that for spectra approximately 90° apart from each other follow the same trend. This symmetry is shown as well in Fig. 4(d), where the Bragg edge heights corresponding to the $\{111\}$, $\{200\}$, and $\{220\}$ lattice planes are plotted versus projection angles. These results were compared with data from conventional neutron diffraction, carried out at the GEM [38] diffractometer at ISIS (UK). Figure 4(a) shows the recalculated pole figures for the same lattice planes evaluated from the orientation distribution function (ODF) obtained from the diffraction measurements. The diffraction pole figures confirm the symmetrical behavior that is observed in the linear attenuation coefficient spectra for the Bragg edge height as a function of the sample rotation. Since the $\{hkl\}$ Bragg edge height is proportional to the number of crystallites having their $\{hkl\}$ planes normal to the incoming beam direction, the projection angle dependent Bragg edge height in a tomography scan can be used to create entries to a pole figure. Figure 4(b) displays the pole figure coverage by our tomographic scan, with values calculated from the Bragg edge heights respective to each of the tomography rotation angles. The rotation angles selected and shown in Fig. 4(c) are also marked with black squares in Fig. 4(a). Both the visual comparison of Figs. 4(a) and 4(b) and the plots in Fig. 4(d), which

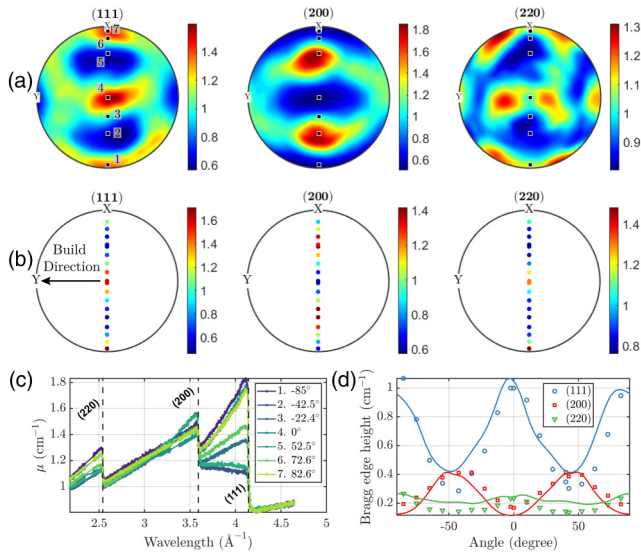


FIG. 4. (a) Pole figures corresponding to the {111}, {200}, and {220} lattice planes, measured at the GEM diffractometer. (b) Corresponding partial pole figures by evaluating the height of the Bragg edges corresponding to the same lattice planes in the bulk sample spectrum, for 19 tomography rotation angles. (c) Bragg edge patterns of the bulk sample for a selection of seven tomography rotation angles. The corresponding angle locations in the pole figures are shown in (a) with black square markers. (d) Bragg edge heights as a function of tomography rotation angles for the {111}, {200}, and {220} lattice planes shown in blue, red, and green colors, are evaluated directly from the tomography Bragg patterns (round markers) and from the neutron diffraction pole figures (thick lines).

displays the pole figure profile along the X axis obtained both by diffraction and by tomography, show quantitatively a very good match. Note that in Fig. 4(b) the magnitudes of the Bragg edge heights are obtained as the relative deviation from the mean height for each lattice plane family respectively, to take into account the contributions from the structure factor for each of the lattice planes. Likewise, in Fig. 4(d) the magnitude of the pole figure values are normalized to the maximum value of the Bragg edge heights for each family of lattice planes. The same approach was adopted for the 3D-LSP processed samples, however, no influence of the LSP treatment on the crystallographic texture was observed.

IV. CONCLUSION

Neutron Bragg edge tomography has been utilized to produce volumetric maps of the planar isotropic strains in 316L stainless steel samples. This was possible due to the isotropic property of the strain in the sample planes orthogonal to the build direction and parallel to the neutron beam, induced by the layer-by-layer nature of the material processing technique. In particular, the effect of the novel 3D-LSP processing technique on the surface strains was studied. A 0.2 mm deep compressive strain region is found with surface CS values approaching $-500 \mu\epsilon$. While still using a very limited number of angular projections, the measurements are in good agreement with the ones obtained with two-dimensional radiographic neutron Bragg edge measurements of the identical samples. Furthermore, the retrieved strain values reproduce the same trends as conventional techniques such as the hole drilling method [29,48,49] and coincide well on an absolute scale, when accounting for different spatial resolutions. The method presented here enables the straightforward analysis and detection of strain variations within the entire sample volume, which are often obscured or cannot be retrieved with single-shot measurements in conventional nondestructive testing methods such as 2D Bragg edge radiography or neutron diffraction. We show that additionally to the strain volumes, the linear attenuation coefficient volumes are obtained with the same data processing workflow. The attenuation contrast exhibits processing defects related to bulk density and allows for their characterization and localization in the sample volume. Furthermore, we found that the processing through the 3D-LSP technique yields a 2% higher bulk density than the as built sample, in the sample region where the laser shock peening is applied. Finally, we show that from the very same measurement, some quantitative conclusions about the crystallographic texture of the sample could be drawn, by analyzing changes in the Bragg edge spectra with the projection angle.

ACKNOWLEDGMENTS

The project was enabled partially through funding from the Strategic Focus Area Advanced Manufacturing (SFA-AM), an initiative of the ETH Board. M.B. acknowledges funding from DanScatt. N.K. and R.L. gratefully acknowledge the generous support of PX Group to the LMTM laboratory. M.S. and T.S. express acknowledgment for granted J-PARC MLF beamtime for Proposal No. 2019A0215.

[1] R. Woracek, J. Santisteban, A. Fedrigo, and M. Strobl, Diffraction in neutron imaging: A review, *Nucl. Instrum. Methods Phys. Res., Sect. A* **878**, 141 (2018).

[2] A. Tremsin and J. Vallergera, Unique capabilities and applications of microchannel plate (MCP) detectors with Medipix/Timepix readout, *Radiat. Meas.* **130**, 106228 (2020).

[3] R. S. Ramadhan, A. K. Syed, A. S. Tremsin, W. Kockelmann, R. Dalgliesh, B. Chen, D. Parfitt, and M. E. Fitzpatrick, Mapping residual strain induced by cold working and by laser shock peening using neutron transmission spectroscopy, *Mater. Design* **143**, 56 (2018).

[4] J. R. Santisteban, A. Steuwer, L. Edwards, P. Withers, and M. Fitzpatrick, Mapping of unstressed lattice parameters using pulsed neutron transmission diffraction, *J. Appl. Crystallogr.* **35**, 497 (2002).

[5] A. Steuwer, P. Withers, J. Santisteban, and L. Edwards, Using pulsed neutron transmission for crystalline phase imaging and analysis, *J. Appl. Phys.* **97**, 074903 (2005).

[6] T. Watkins, H. Bilheux, K. An, A. Payzant, R. Dehoff, C. Duty, W. Peter, C. Blue, and C. A. Brice, Neutron characterization for additive manufacturing, *Adv. Mater. Process.* **171**, 23 (2013).

- [7] J. Santisteban, M. Vicente-Alvarez, P. Vizcaino, A. Banchik, S. Vogel, A. Tremsin, J. Vallergera, J. McPhate, E. Lehmann, and W. Kockelmann, Texture imaging of zirconium based components by total neutron cross-section experiments, *J. Nucl. Mater.* **425**, 218 (2012).
- [8] R. Woracek, D. Penumadu, N. Kardjilov, A. Hilger, M. Boin, J. Banhart, and I. Manke, Neutron Bragg edge tomography for phase mapping, *Phys. Proc.* **69**, 227 (2015).
- [9] C. M. Wensrich, J. N. Hendriks, A. Gregg, M. H. Meylan, V. Luzin, and A. S. Tremsin, Bragg-edge neutron transmission strain tomography for *in situ* loadings, *Nucl. Instrum. Methods Phys. Res., Sect. B* **383**, 52 (2016).
- [10] H. J. Kirkwood, S. Y. Zhang, A. S. Tremsin, A. M. Korsunsky, N. Baimpas, and B. Abbey, Neutron strain tomography using the radon transform, *Mater. Today: Proc.* **2**, S414 (2015).
- [11] J. N. Hendriks, A. W. T. Gregg, R. R. Jackson, C. M. Wensrich, A. Wills, A. S. Tremsin, T. Shinohara, V. Luzin, and O. Kirstein, Tomographic reconstruction of triaxial strain fields from Bragg-edge neutron imaging, *Phys. Rev. Mater.* **3**, 113803 (2019).
- [12] S. Pratihari, M. Turski, L. Edwards, and P. Bouchard, Neutron diffraction residual stress measurements in a 316L stainless steel bead-on-plate weld specimen, *Int. J. Pressure Vessels Piping* **86**, 13 (2009).
- [13] F. Martina, M. Roy, B. Szost, S. Terzi, P. A. Colegrove, S. W. Williams, P. Withers, J. Meyer, and M. Hofmann, Residual stress of as-deposited and rolled wire+arc additive manufacturing Ti-6Al-4V components, *Mater. Sci. Technol.* **32**, 1439 (2016).
- [14] Z. Wang, E. Denlinger, P. Michaleris, A. D. Stoica, D. Ma, and A. M. Beese, Residual stress mapping in Inconel 625 fabricated through additive manufacturing: Method for neutron diffraction measurements to validate thermomechanical model predictions, *Mater. Design* **113**, 169 (2017).
- [15] W. Woo, J. Jeong, D.-K. Kim, C. Lee, S.-H. Choi, J.-Y. Suh, S. Lee, S. Harjo, and T. Kawasaki, Stacking fault energy analyses of additively manufactured stainless steel 316L and CrCoNi medium entropy alloy using *in situ* neutron diffraction, *Sci. Rep.* **10**, 1350 (2020).
- [16] R. J. Williams, F. Vecchiato, J. Kelleher, M. R. Wenman, P. A. Hooper, and C. M. Davies, Effects of heat treatment on residual stresses in the laser powder bed fusion of 316L stainless steel: Finite element predictions and neutron diffraction measurements, *J. Manuf. Process.* **57**, 641 (2020).
- [17] E. Polatidis, J. Čapek, A. Arabi-Hashemi, C. Leinenbach, and M. Strobl, High ductility and transformation-induced-plasticity in metastable stainless steel processed by selective laser melting with low power, *Scr. Mater.* **176**, 53 (2020).
- [18] J. Čapek, E. Polatidis, M. Knapek, C. Lyphout, N. Casati, R. Pederson, and M. Strobl, The effect of γ'' and δ phase precipitation on the mechanical properties of Inconel 718 manufactured by selective laser melting: An *in situ* neutron diffraction and acoustic emission study, *JOM* **73**, 223 (2021).
- [19] P. Trtik, Neutron microtomography of voids in gold, *MethodsX* **4**, 492 (2017).
- [20] F. Grazzi, C. Cialdai, M. Manetti, M. Massi, M. P. Morigi, M. Bettuzzi, R. Brancaccio, F. Albertin, T. Shinohara, T. Kai *et al.*, A multi-technique tomography-based approach for non-invasive characterization of additive manufacturing components in view of vacuum/UHV applications: Preliminary results, *Rend. Lincei Sci. Fis. Nat.* **32**, 463 (2021).
- [21] A. J. Brooks, J. Ge, M. M. Kirka, R. R. Dehoff, H. Z. Bilheux, N. Kardjilov, I. Manke, and L. G. Butler, Porosity detection in electron beam-melted Ti-6Al-4V using high-resolution neutron imaging and grating-based interferometry, *Progr. Additive Manuf.* **2**, 125 (2017).
- [22] A. J. Brooks, H. Yao, J. Yuan, O. Kio, C. G. Lowery, H. Markötter, N. Kardjilov, S. Guo, and L. G. Butler, Early detection of fracture failure in SLM AM tension testing with Talbot-Lau neutron interferometry, *Additive Manuf.* **22**, 658 (2018).
- [23] M. Bacak, J. Valsecchi, J. Čapek, E. Polatidis, A. Kaestner, A. Arabi-Hashemi, I. Kruk, C. Leinenbach, A. Long, A. Tremsin *et al.*, Neutron dark-field imaging applied to porosity and deformation-induced phase transitions in additively manufactured steels, *Mater. Design* **195**, 109009 (2020).
- [24] M.-E. Lăcătușu, L. T. Kuhn, R. E. Johnsen, P. K. Tung, S. Schmidt, T. Shinohara, R. Kiyonagi, A. S. Tremsin, N. Elewa, R. Woracek *et al.*, A multimodal operando neutron study of the phase evolution in a graphite electrode, [arXiv:2104.03564](https://arxiv.org/abs/2104.03564).
- [25] C. Li, Z. Liu, X. Fang, and Y. Guo, Residual stress in metal additive manufacturing, *Proc. CIRP* **71**, 348 (2018).
- [26] N. Kalentics, E. Boillat, P. Peyre, S. Čirić-Kostić, N. Bogojević, and R. E. Logé, Tailoring residual stress profile of selective laser melted parts by laser shock peening, *Additive Manuf.* **16**, 90 (2017).
- [27] N. Kalentics, K. Huang, M. O. V. de Seijas, A. Burn, V. Romano, and R. E. Logé, Laser shock peening: A promising tool for tailoring metallic microstructures in selective laser melting, *J. Mater. Process. Technol.* **266**, 612 (2019).
- [28] N. Kalentics, M. O. V. de Seijas, S. Griffiths, C. Leinenbach, and R. E. Logé, 3D laser shock peening—A new method for improving fatigue properties of selective laser melted parts, *Additive Manuf.* **33**, 101112 (2020).
- [29] N. Kalentics, E. Boillat, P. Peyre, C. Gorny, C. Kenel, C. Leinenbach, J. Jhabvala, and R. E. Logé, 3D laser shock peening—A new method for the 3D control of residual stresses in selective laser melting, *Mater. Design* **130**, 350 (2017).
- [30] M. Morgano, N. Kalentics, C. Carminati, J. Čapek, M. Makowska, R. Woracek, T. Maimaitiyili, T. Shinohara, R. Logé, and M. Strobl, Investigation of the effect of laser shock peening in additively manufactured samples through Bragg edge neutron imaging, *Additive Manuf.* **34**, 101201 (2020).
- [31] M. Busi, N. Kalentics, M. Morgano, S. Griffiths, A. S. Tremsin, T. Shinohara, R. Logé, C. Leinenbach, and M. Strobl, Non-destructive characterization of laser powder bed fusion parts with neutron Bragg edge imaging, *Additive Manuf.* **39**, 101848 (2021).
- [32] B. Clausen, T. Lorentzen, and T. Leffers, Self-consistent modelling of the plastic deformation of fcc polycrystals and its implications for diffraction measurements of internal stresses, *Acta Mater.* **46**, 3087 (1998).
- [33] P. Withers, M. Preuss, A. Steuwer, and J. Pang, Methods for obtaining the strain-free lattice parameter when using diffraction to determine residual stress, *J. Appl. Crystallogr.* **40**, 891 (2007).
- [34] T. Shinohara, T. Kai, K. Oikawa, T. Nakatani, M. Segawa, K. Hiroi, Y. Su, M. Ooi, M. Harada, H. Iikura *et al.*, The energy-

- resolved neutron imaging system, RADEN, *Rev. Sci. Instrum.* **91**, 043302 (2020).
- [35] T. Kohler, A projection access scheme for iterative reconstruction based on the golden section, in *IEEE Symposium Conference Record Nuclear Science 2004* (IEEE, New York, 2004), Vol. 6, pp. 3961–3965.
- [36] A. P. Kaestner, B. Munch, and P. Trtik, Spatiotemporal computed tomography of dynamic processes, *Opt. Eng.* **50**, 123201 (2011).
- [37] A.-H. Puichaud, C. Flament, A. Chniouel, F. Lomello, E. Rouesne, P.-F. Giroux, H. Maskrot, F. Schuster, and J.-L. Béchade, Microstructure and mechanical properties relationship of additively manufactured 316L stainless steel by selective laser melting, *EPJ Nucl. Sci. Technol.* **5**, 23 (2019).
- [38] W. Kockelmann, L. Chapon, and P. Radaelli, Neutron texture analysis on GEM at ISIS, *Phys. B: Condens. Matter* **385-386**, 639 (2006).
- [39] L. Lutterotti Jr., S. Matthies, H.-R. Wenk, A. Schultz, and J. Richardson Jr., Combined texture and structure analysis of deformed limestone from time-of-flight neutron diffraction spectra, *J. Appl. Phys.* **81**, 594 (1997).
- [40] F. Bachmann, R. Hielscher, and H. Schaeben, Texture analysis with mtex-free and open source software toolbox, in *Solid State Phenomena* (Trans Tech, Switzerland, 2010), Vol. 160, pp. 63–68.
- [41] W. van Aarle, W. J. Palenstijn, J. Cant, E. Janssens, F. Bleichrodt, A. Dabrovolski, J. De Beenhouwer, K. J. Batenburg, and J. Sijbers, Fast and flexible x-ray tomography using the ASTRA toolbox, *Opt. Express* **24**, 25129 (2016).
- [42] C. Carminati, M. Strobl, T. Minniti, P. Boillat, J. Hovind, M. Morgano, T. Holm Rod, E. Polatidis, J. Valsecchi, D. Mannes *et al.*, Bragg-edge attenuation spectra at voxel level from 4D wavelength-resolved neutron tomography, *J. Appl. Crystallogr.* **53**, 188 (2020).
- [43] M. Busi, N. Kalentics, M. Morgano, S. Griffiths, A. S. Tremsin, T. Shinohara, R. Logé, C. Leinenbach, and M. Strobl, A parametric neutron Bragg edge imaging study of additively manufactured samples treated by laser shock peening, *Sci. Rep.* **11**, 14919 (2021).
- [44] E. Garlea, H. Choo, C. Sluss, M. Koehler, R. Bridges, X. Xiao, Y. Ren, and B. Jared, Variation of elastic mechanical properties with texture, porosity, and defect characteristics in laser powder bed fusion 316L stainless steel, *Mater. Sci. Eng. A* **763**, 138032 (2019).
- [45] A. du Plessis, D. Glaser, H. Moller, N. Mathe, L. Tshabalala, B. Mfusi, and R. Mostert, Pore closure effect of laser shock peening of additively manufactured AlSi10Mg, *3D Print. Additive Manuf.* **6**, 245 (2019).
- [46] S.-H. Sun, K. Hagihara, and T. Nakano, Effect of scanning strategy on texture formation in Ni-25 at.% Mo alloys fabricated by selective laser melting, *Mater. Design* **140**, 307 (2018).
- [47] L. Thijs, K. Kempen, J.-P. Kruth, and J. Van Humbeeck, Fine-structured aluminium products with controllable texture by selective laser melting of pre-alloyed AlSi10Mg powder, *Acta Mater.* **61**, 1809 (2013).
- [48] A. S. Wu, D. W. Brown, M. Kumar, G. F. Gallegos, and W. E. King, An experimental investigation into additive manufacturing-induced residual stresses in 316L stainless steel, *Metall. Mater. Trans. A* **45**, 6260 (2014).
- [49] D. Brown, J. Bernardin, J. Carpenter, B. Clausen, D. Spornjak, and J. Thompson, Neutron diffraction measurements of residual stress in additively manufactured stainless steel, *Mater. Sci. Eng. A* **678**, 291 (2016).